

Research Article

Boosting peroxidase-like activity of Fe/Mn-N-C dual-single-atom nanozyme for colorimetric assay of total antioxidant capacity

 Bingsong Yan[#], Yuanjie Zhang[#], Yizhong Lu^{*}, Zongming Liu^{*}, Jinkai Li^{*}

School of Materials Science and Engineering, University of Jinan, Jinan 250022, China

ARTICLE INFO

Keywords:

 Single-atom nanozyme
 Peroxidase-like
 Colorimetric analysis
 TAC
 Smartphone

ABSTRACT

Total antioxidant capacity (TAC) quantification is pivotal for biomedical diagnostics and food quality control. Herein, we developed a smartphone-integrated colorimetric platform leveraging a Fe-Mn dual-single-atom nanozyme (Fe/Mn-N-C) with enhanced peroxidase-like activity. Density functional theory calculations revealed that the unique diatomic synergy reduced the energy barrier during the catalytic process, thus endowing Fe/Mn-N-C with superior peroxidase-like activity. The inhibition mechanism of different types of antioxidants on the color reaction was investigated. The system quantified AA via antioxidant-induced suppression of oxTMB formation and applied successfully to the TAC detection of several fruit juices and commercial beverages. This work provided a new perspective for designing advanced single-atom nanozyme and developed a low-cost and easy-to-operate TAC detection strategy with good sensitivity and specificity.

1. Introduction

Total Antioxidant Capacity (TAC) reflects the cumulative effect of all antioxidants (e.g., glutathione (GSH) and ascorbic acid (AA) etc.) in a biological system, and serves as a pivotal indicator for diagnosing oxidative stress-related diseases and evaluating the quality of foods and drugs [1]. Currently, there are numerous methods for detecting TAC, such as electrochemical, chemiluminescence and chromatographic methods. However, these methods involve complex operational procedures, failing to achieve visual detection, and require the support of large-scale equipment [2–4]. These limitations impede their deployment in resource-constrained environments or practical applications, underscoring an urgent need for sensitive, rapid, and cost-effective alternative solutions.

Nanozymes, catalytic nanomaterials that mimic the properties of natural enzymes, have attracted considerable interest in nanosensing and biomedicine as stable and tunable substitutes for natural enzymes [5]. Among them, single-atom nanozymes (SAzymes) represent a promising class of artificial biomimetic enzymes, featuring maximized atomic utilization efficiency, uniform active sites and exceptional catalytic activity [6]. However, single-metal SAzymes (e.g., Mn-N-C or Fe-N-C) are often restricted to substrate affinity and exhibit suboptimal reaction kinetics due to their simplistic electronic structures [7]. Rational design of poly-metallic active centers enables effective modulation of local electronic structures, synergistically enhancing the enzyme-mimicking activity of

M-N-C nanozymes to advance analytical performance in biosensing platforms [8]. Accordingly, engineering single-atom nanozymes with poly-metallic sites represents a promising strategy for sensitive TAC monitoring, while providing new mechanistic insights into nanozymes catalysis.

Herein, a Fe-Mn dual-single-atom nanozyme (Fe/Mn-N-C) was constructed within a zeolitic imidazolate framework-derived nitrogen-carbon matrix using a cage-confined synthesis strategy. Density functional theory calculations elucidated that the unique diatomic synergy effectively promoted the adsorption of H₂O₂ and subsequent catalytic turnover, thereby endowing the prepared nanozyme with superior peroxidase-like activity. Leveraging the enhanced activity, a smartphone-based colorimetric biosensor incorporating an RGB quantification model for TAC analysis was developed. The platform achieved precise TAC determination in complex food matrices, including fresh fruits and commercial beverages. This study provided an innovative sensing platform for efficient TAC detection and opening new avenues for the application of SAzymes in biosensing.

2. Materials and methods

2.1. Materials and reagents

Diammonium 2,2'-azino-bis(3-ethylbenzothiazoline-6-sulfonate) (ABTS), 3,3',5,5'-tetramethylbenzidine (TMB), potassium thiocyanate (KSCN), nitrotetrazolium chloride blue (NBT), glutathione, L-lysine,

* Corresponding authors.

E-mail addresses: mse_luyz@ujn.edu.cn (Y. Lu), liuzm@ujn.edu.cn (Z. Liu), mse_lijk@ujn.edu.cn (J. Li).

These authors contributed equally to this work.

L-threonine, L-isoleucine, o-phenylenediamine (OPD), L-arginine and anhydrous sodium acetate were purchased from Macklin Company. Ferrous bisglycinate, 2-methylimidazole, thiourea, gallic acid and triphenylphosphine were purchased from Aladdin Reagent Co., Ltd. Potassium chloride (KCl), L-tyrosine, lactose, maltose, fructose and hydrogen peroxide were purchased from Sinopharm Chemical Reagent Co., LTD. Sodium chloride (NaCl), acetic acid and methanol were purchased from Tianjin Fuyu Fine Chemical Co., LTD. Zinc nitrate hexahydrate ($\text{Zn}(\text{NO}_3)_2 \cdot 6\text{H}_2\text{O}$) was purchased from Xilong Scientific Co., Ltd. Glucose, soluble starch and calcium nitrate tetrahydrate ($\text{Ca}(\text{NO}_3)_2 \cdot 4\text{H}_2\text{O}$) were purchased from Tianjin Damao chemical reagent factory. Deionized water was used during the experiment. Anhydrous magnesium sulfate ($\text{Mg}(\text{SO}_4)_2$) was purchased from Tianjin Hengxing Chemical reagent manufacturing Co., LTD.

2.2. Instruments

Field emission scanning electron microscopy (SEM) images were observed with Gemini300 (ZEISS, Germany). Transmission electron microscopy (TEM) images were observed with JEM-2100F (JEOL, Japan). Aberration-corrected high-angle annular dark-field scanning transmission electron microscopy (HAADF-STEM) images were performed with

a high resolution transmission electron microscope operated at 200 kV with spherical aberration corrected under HAADF-STEM mode (Titan Themis G2 60–300, Thermo Fisher, USA). The powder X-ray diffraction (XRD) pattern was obtained by SmartLab 9KW (Rigaku, Japan). X-ray photoelectron spectroscopy (XPS) analysis was performed using the Thermo Fischer, ESCALAB Xi+ instrument. Fourier transform infrared spectroscopy (FTIR) spectrometer spectra were recorded using Nicolet iS10 (ThermoFisher Scientific, USA). Raman spectra were obtained by Horiba LabRAM HR Evolution. UV–visible spectroscopy and enzyme kinetics tests were collected using a UV-6100 spectrophotometer (Metash, China).

3. Results and discussion

3.1. Synthesis and characterization of Fe/Mn-N-C

In this work, Mn-doped ZIF-8 frameworks were engineered as nanoscale cages to adsorb and confine sublimated ferrocene (FeCp_2) vapor through an impregnation strategy. Following pyrolysis at 900 °C, the Fe/Mn-ZIF-8 precursor was converted into Fe/Mn-N-C, featuring atomically dispersed metal sites within a hierarchical carbon matrices (Fig. 1(a)). The SEM image depicted the precursor Fe/Mn-ZIF-8

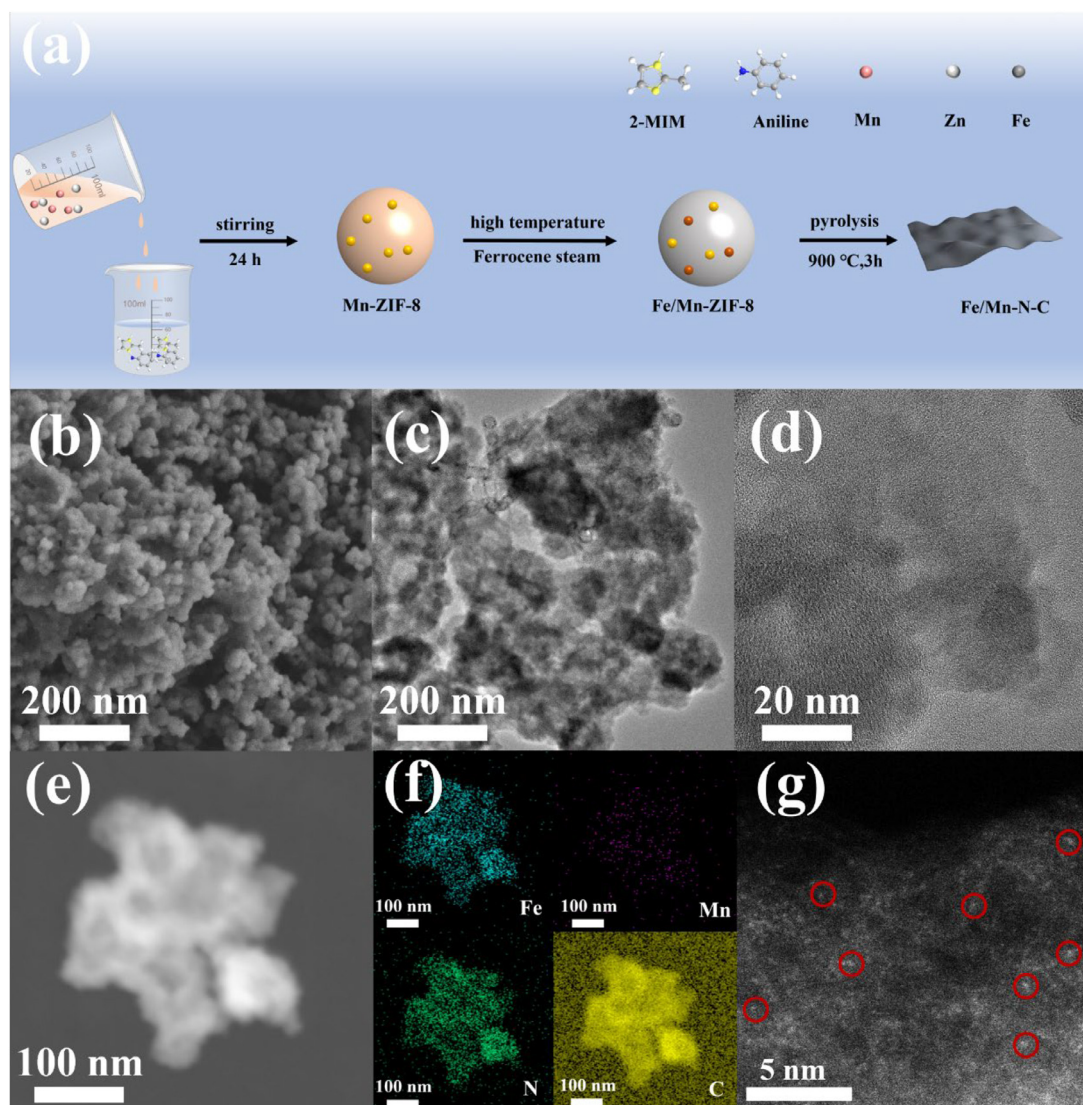


Fig. 1. (a) Schematic of the cage-confinement strategy for synthesizing Fe/Mn-N-C, (b) SEM image of Fe/Mn-N-C, (c)(d) TEM images of Fe/Mn-N-C, (e) STEM image, (f) corresponding EDS elemental mapping images, (g) aberration-corrected HAADF-STEM image of Fe/Mn-N-C.

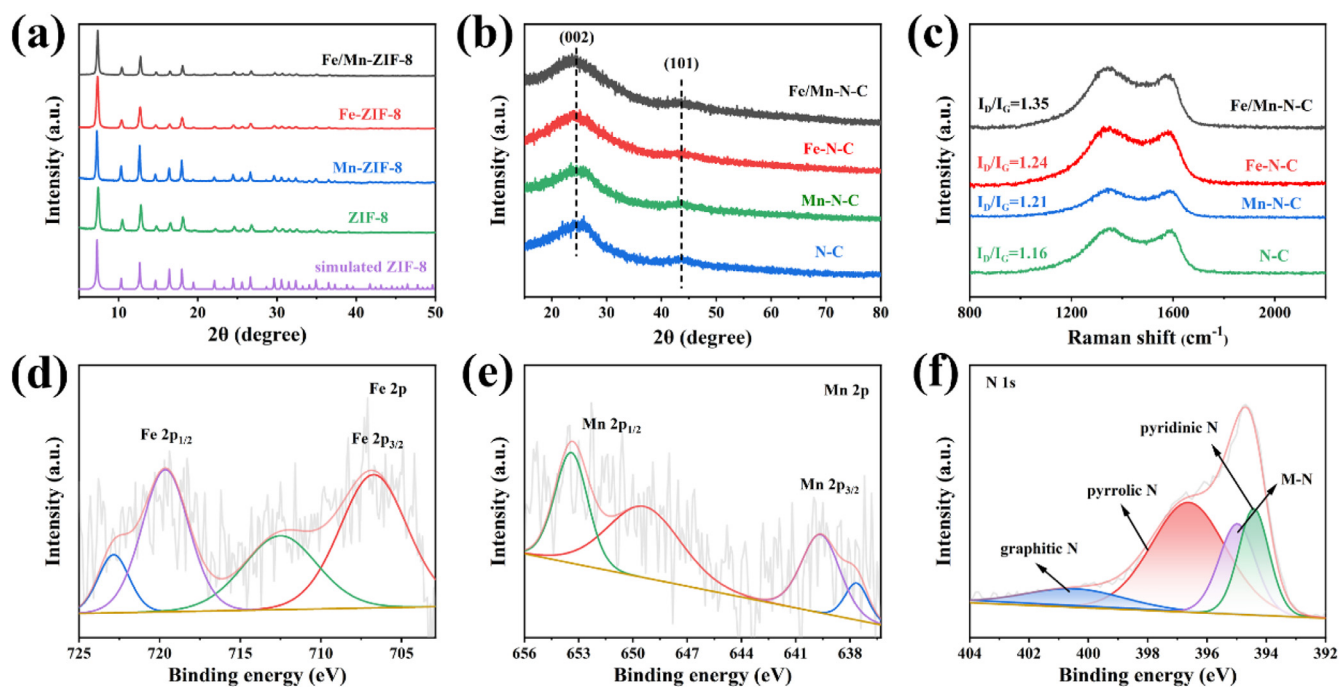


Fig. 2. (a) XRD patterns of four precursors and simulated ZIF-8. (b) XRD patterns, (c) Raman spectra of four derivatives after pyrolysis. High-resolution XPS spectra of (d) Fe 2p, (e) Mn 2p and (f) Fe 2p in Fe/Mn-N-C.

with typical spherical morphology attributed to the presence of aniline (Fig. 1(b)) [9]. The morphology of Fe/Mn-N-C was further characterized by TEM, revealing its typical nanosheet structure (Fig. 1(c)). Moreover, Fig. 1(d) indicated the absence of distinct iron and manganese metal nanoparticles or clusters. STEM image (Fig. 1(e)) and corresponding EDS elemental mapping images (Fig. 1(f)) demonstrated the uniform distribution of Fe, Mn, N and C within Fe/Mn-N-C, confirming the successful synthesis of the material. Further, the aberration-corrected HAADF-STEM with atomic-resolution displayed only tiny and bright spots on the carbon support, which were identified as uniform dispersed single atoms (Fig. 1(g)). The above test results indicated that the successful preparation of Fe/Mn-N-C.

The crystal structures of the four precursors were examined by XRD. As depicted in Fig. 2(a), the XRD patterns of ZIF-8, Mn-ZIF-8, Fe-ZIF-8, and Fe/Mn-ZIF-8 exhibited close resemblance with the simulated pattern of ZIF-8, which confirming their successful synthesis and high phase purity. This indicated that neither chemical doping of Mn nor gas-phase adsorption of FeCp altered the crystalline framework of ZIF-8. Correspondingly, XRD analysis of the pyrolyzed derivatives were conducted. The XRD spectra (Fig. 2(b)) revealed characteristic diffraction peaks at 24.5° and 43.4° of four catalysts, attributed to (002) and (101) crystalline planes from carbon. Notably, the XRD patterns showed no evidence of discernible crystalline phases from iron or manganese nanoparticles, which is fully consistent with the TEM observations that indicated a highly dispersed state of the metal species.

Further analysis using Raman spectroscopy explored the impact of iron and manganese doping on the porous carbon materials. Fig. 2(c) showed that all catalysts exhibited two characteristic Raman bands: the D band at 1343 cm⁻¹ and the G band at 1575 cm⁻¹, corresponding to disordered carbon and graphitic carbon, respectively [10]. The intensity ratio (I_D/I_G) of the D and G bands for Fe/Mn-N-C is 1.35, higher than that of the other three catalysts, indicating that co-doping of iron and manganese may facilitated the formation of disordered carbon during the pyrolysis process [11]. Furthermore, XPS was employed to probe the chemical states of surface elements in the Fe/Mn-N-C, uncovering insights into its exceptional catalytic properties. The Fe 2p spectrum of Fe/Mn-N-C exhibited two characteristic binding energy peaks centered

at 719.6 and 706.8 eV, corresponding to Fe 2p_{1/2} and Fe 2p_{3/2} orbitals respectively (Fig. 2d). This indicated the predominant coexistence of two distinct iron chemical states in catalyst, which are related to the spin-orbit splitting of Fe 2p [12]. Analogously, the Mn 2p region displayed a well-resolved spin-orbit doublet centered at 653.4 eV (2p_{1/2}) and 639.7 eV (2p_{3/2}), confirming the characteristic electronic configuration of manganese in the material (Fig. 2(e)). Analysis of the N 1s spectrum (Fig. 2(f)) revealed peaks at 400.7, 396.6, 395.0 and 394.4 eV, attributed to graphitic nitrogen, pyrrolic nitrogen, M-N and pyridinic nitrogen. Graphitic nitrogen could enhance substrate adsorption, while pyridinic nitrogen facilitated H₂O₂ capture and protonation, which was beneficial for catalytic reaction [13]. According to the ICP-OES result, the Fe and Mn loading in Fe/Mn-N-C are 3.67 wt% and 0.037 wt%, respectively.

3.2. POD activity of Fe/Mn-N-C

As shown in Fig. 3(a), the peroxidase-like activity of Fe/Mn-N-C was evaluated using different chromogenic substrates. In the presence of H₂O₂, solutions of ABTS, OPD, and TMB chromogenic substrates co-existing with Fe/Mn-N-C were catalytically oxidized to green, yellow, and blue colors, respectively, with characteristic absorption peaks at 416, 448, and 652 nm. Under the identical conditions, Fe/Mn-N-C rapidly oxidized TMB to be blue with pronounced absorbance at 652 nm accompanied with H₂O₂. Furthermore, the mixed solution remained colorless without catalyst, while a weaker blue color was observed in the absence of H₂O₂ (Fig. 3(b)). This confirmed that Fe/Mn-N-C possessed outstanding POD-like catalytic performance and weaker oxidase-like activity. The catalytic performance of Fe/Mn-N-C could be limited to several factors including pH, TMB concentration, H₂O₂ concentration, catalyst concentration, incubation temperature, and incubation time. Reaction parameters were systematically optimized, revealing maximal enzymatic activity was achieved toward pH = 4, 0.20 mM, 2.0 mM, 3 μg/mL, 25 °C and 10 min under standardized assay conditions (Fig. S1(a)–(f)). The POD-like activities of four synthesized catalysts were systematically evaluated using TMB as the substrate. The Fe/Mn-N-C achieved a maximal specific activity of 0.0401 U/mg, representing 1.86-

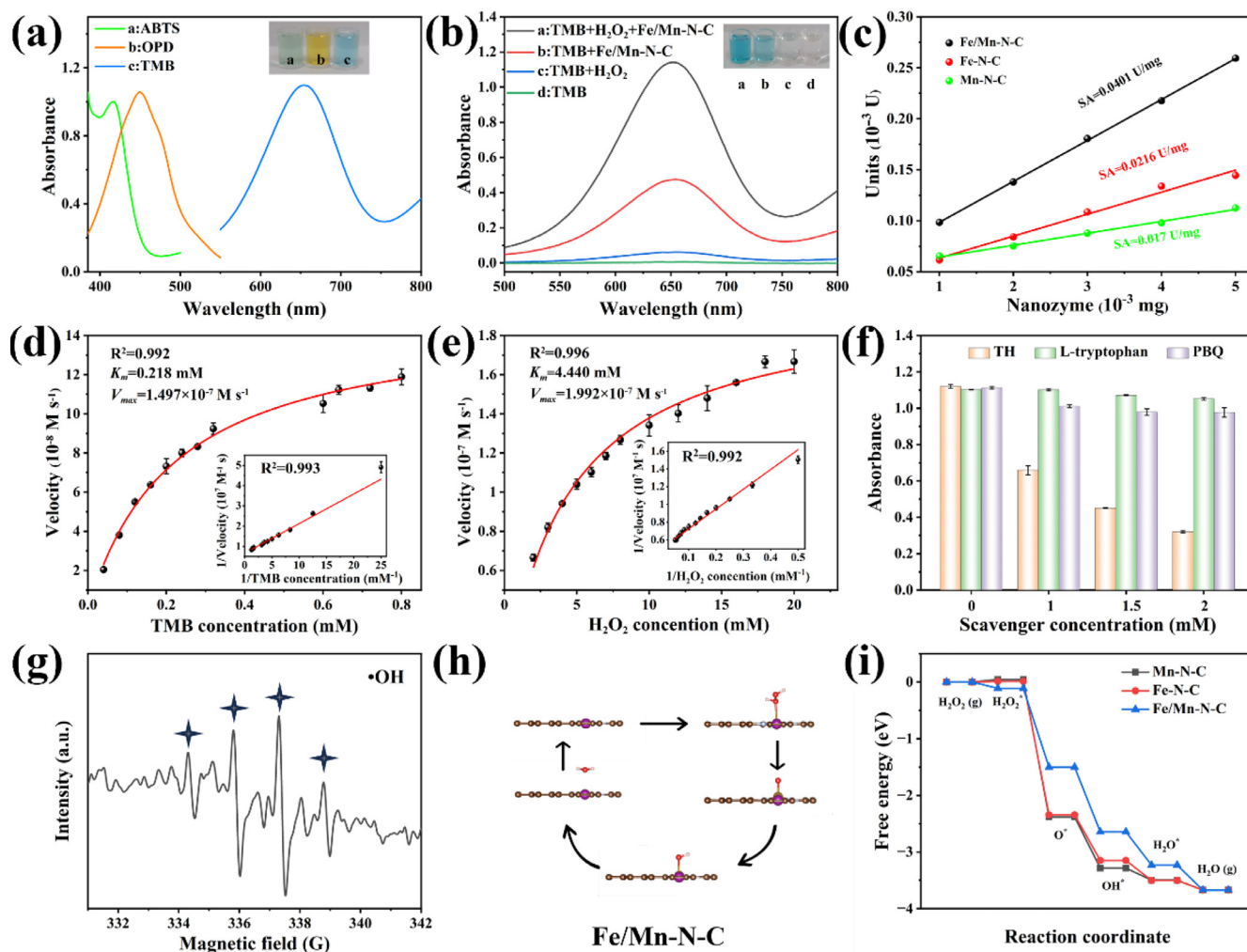


Fig. 3. (a) UV–Vis absorption spectra of Fe/Mn-N-C catalyzing the oxidation of chromogenic substrates. (b) UV–Vis absorption spectra of different reaction systems. (c) Specific activity of three nanozymes. The steady-state kinetic analysis curves and the corresponding Lineweaver-Burk plots of Fe/Mn-N-C obtained by varying the concentrations of (d) TMB and (e) H_2O_2 . (f) Absorbance of the Fe/Mn-N-C/ H_2O_2 /TMB system in the presence of different scavengers. (g) EPR spectra of DMPO solution in the Fe/Mn-N-C/ H_2O_2 /TMB system. (h) Schematic of the proposed reaction process for the Fe/Mn-N-C. (i) Free energy diagrams of POD-like on three nanozymes. (Error bar represents the standard deviation of three independent measurements).

fold and 2.36-fold enhancements over Fe-N-C (0.0216 U/mg) and Mn-N-C (0.0170 U/mg, respectively) (Fig. 3(c)). The observed activity enhancement likely originated from interatomic synergy within the dual-metal centers, substantially boosting the catalytic efficiency of nanozyme [14].

The steady-state kinetic experiments were conducted to further investigate the catalytic efficiency of Fe/Mn-N-C under optimized conditions. Fig. 3(d)(e) shown the catalytic kinetics of Fe/Mn-N-C toward TMB and H_2O_2 followed the well-known Michaelis-Menten equation. From the Lineweaver-Burk plot of TMB, it was found the maximum reaction rate (V_{\max}) for TMB is $1.497 \times 10^7 \text{ M s}^{-1}$, with a Michaelis constant (K_m) of 0.218 mM. Similarly, the V_{\max} and K_m values for H_2O_2 were determined to be $1.992 \times 10^{-7} \text{ M s}^{-1}$ and 4.44 mM. Typically, K_m is considered an indicator of enzyme-substrate affinity, where lower values indicate higher affinity [15]. Comparison of K_m and V_{\max} values of Fe/Mn-N-C nanozyme with other reported peroxidase enzymes (Table S1) revealed it has smaller K_m and larger V_{\max} , indicating that Fe/Mn-N-C possessed admirable enzymatic activity. During peroxidase-mimetic catalysis of H_2O_2 , reactive oxygen species (ROS) including hydroxyl radicals ($\bullet\text{OH}$), superoxide anions ($\text{O}_2^{\bullet-}$), and singlet oxygen ($^1\text{O}_2$) are usually generated as key reactive intermediates. Established strategies employed radical-specific scavengers to quench reactive oxygen species generated during nanozyme catalysis, thereby sup-

pressing chromogenic substrate oxidation. To investigate the types of ROS produced by Fe/Mn-N-C during TMB oxidation, thiourea (TH), L-tryptophan, and p-benzoquinone (PBQ) were used to scavenge $\bullet\text{OH}$, $^1\text{O}_2$ and $\text{O}_2^{\bullet-}$. Fig. 3(f) demonstrated that neither L-tryptophan nor PBQ significantly altered the 652 nm absorbance relative to the blank, indicating undetectable generation of $^1\text{O}_2$ and $\text{O}_2^{\bullet-}$ during catalysis. Conversely, TH caused dose-dependent suppression of oxTMB formation, confirming the production of $\bullet\text{OH}$. This established a peroxidase-like catalytic mechanism where Fe/Mn-N-C activated H_2O_2 to generate highly oxidative $\bullet\text{OH}$ species, subsequently oxidizing colorless TMB to blue. Direct evidence of $\bullet\text{OH}$ production was obtained through EPR spin-trapping experiments, with the characteristic 1:2:2:1 quartet spin confirming the radical pathway proposed in scavenger studies (Fig. 3(g)).

To provide atomic-level insights into the peroxidase-like mechanism, the density functional theory calculations were conducted, building upon the experimental characterization. This catalytic mechanism involved H_2O_2 adsorption followed by heterolytic cleavage ($^*\text{H}_2\text{O}_2 \rightarrow ^*\text{O} + \text{H}_2\text{O}$) (Fig. 3(h)). Upon adsorption, H_2O_2 underwent heterolytic scission to form a key $^*\text{O}$ intermediate with concomitant water release. The adsorbed $^*\text{O}$ underwent gradual protonation through continuous hydrogen transfer, culminating in the formation and desorption of $^*\text{H}_2\text{O}$, completing the catalytic cycle. It was noteworthy that within

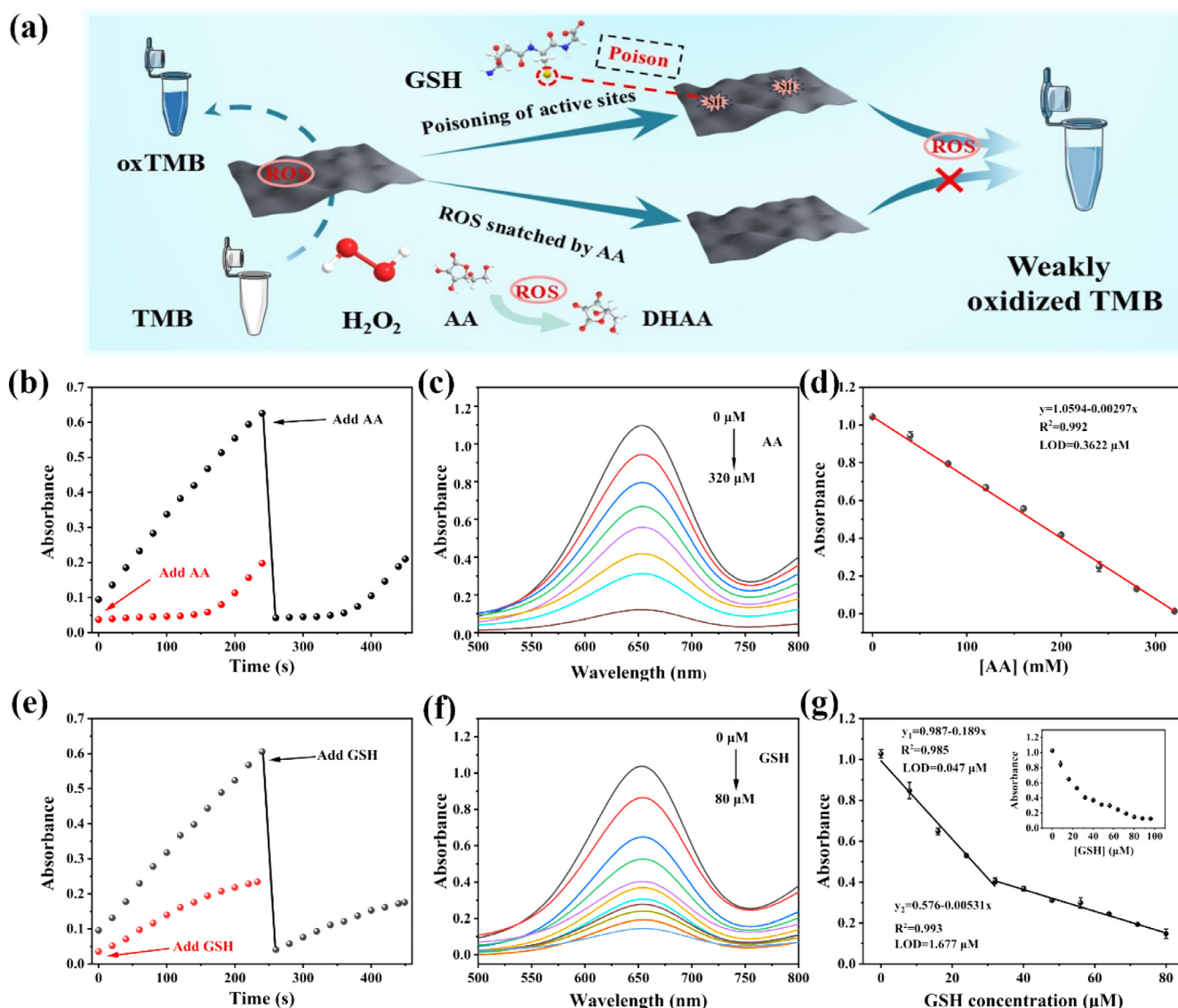


Fig. 4. (a) Schematic diagram of AA and GSH sensing, the inhibitory effects of (b) AA and (e) GSH on TMB oxidation, UV-visible absorption spectra of the Fe/Mn-N-C colorimetric system at various concentrations of (c) AA and (f) GSH. Panels (d) and (g) depict the linear relationship between AA concentration and the absorbance at 652 nm, as well as between GSH concentration and the absorbance at 652 nm. (Error bar represents the standard deviation of three independent measurements).

this catalytic cycle, H_2O_2 adsorption constituted the rate-determining step (RDS) (Fig. 3(i)). In contrast with Mn-N-C (0.0436 eV) and Fe-N-C (0.0114 eV), H_2O_2 adsorption at Fe/Mn-N-C demonstrated superior thermodynamic favorability with a reduced energy barrier (-0.112 eV), facilitating efficient generation of the $\cdot\text{O}$ intermediate and subsequent catalytic turnover. This significantly improved H_2O_2 adsorption capability on Fe/Mn-N-C directly translated into improved POD-like efficiency, which is highly consistent with the catalytic performance measurements.

3.3. Colorimetric detection of AA and GSH

As fundamental biological antioxidants, AA and GSH play indispensable roles in oxidative stress management for clinical diagnostics, therapeutic interventions, and food quality preservation [16]. Leveraging concentration-dependent chromogenic suppression in the Fe/Mn-N-C/TMB/ H_2O_2 system, we developed a colorimetric platform enabling rapid, simultaneous quantification of AA and GSH with excellent sensitivity (Fig. 4(a)). Notably, the spectroscopic analyses revealed distinct inhibitory mechanisms for AA and GSH in suppressing the TMB chro-

mogenic reaction. The inhibitory effects of AA and GSH on the Fe/Mn-N-C catalyzed TMB- H_2O_2 reaction were implemented to investigate by the quenching kinetics experiments. Following the incorporation of AA to the pre-reacted system, a rapid decline in 652 nm absorbance confirmed an effective reduction for oxTMB (Fig. 4(b)). Time-dependent absorption spectra revealed that the slope remained unchanged during the reaction, but the intensity buildup was significantly delayed. This AA-induced inhibition was attributed to the ROS catalyzed by Fe/Mn-N-C preferentially react with AA before TMB oxidation, thereby introducing a distinct lag phase in chromogenesis. In contrast, the TMB oxidation reaction exhibited no temporal delay but demonstrated a significantly decrease in reaction rates (Fig. 4(e)). This inhibition arose from the preferential coordination of the sulfhydryl group of GSH to the metal centers in Fe/Mn-N-C. The binding interaction significantly attenuated the efficiency of ROS production and consequently diminished overall catalytic activity.

Capitalizing on the elucidated inhibition mechanisms, a colorimetric quantification platform for AA and GSH was established. Fig. 4(c) revealed the progressive attenuation of the absorbance at 652 nm was proportional to AA concentration. The system exhibited excellent lin-

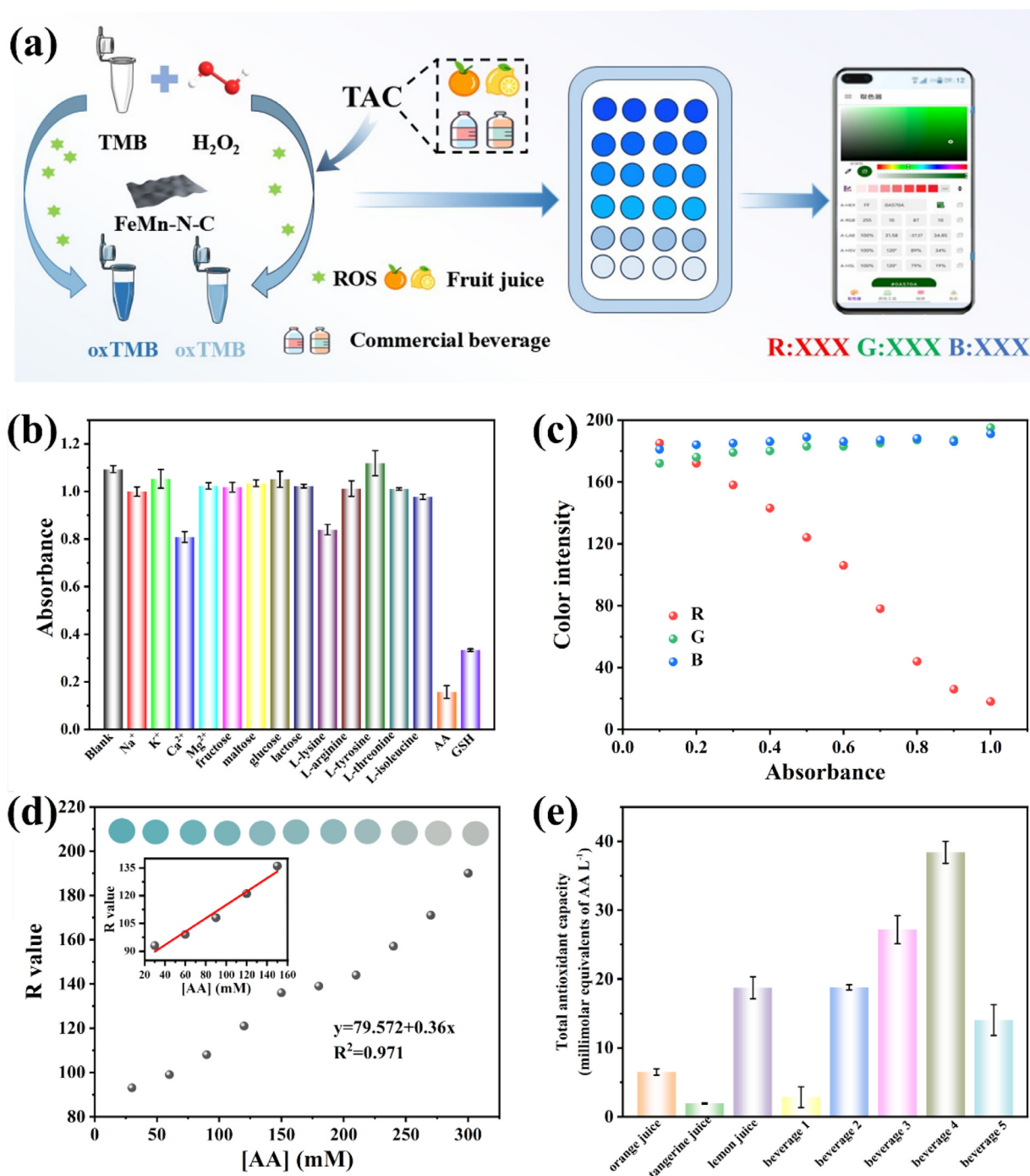


Fig. 5. (a) Schematic diagram of TAC sensing based on Fe/Mn-N-C, (b) selectivity for colorimetric detection of TAC, (c) the RGB values during the absorbance changes, (d) the linear plot of AA concentrations vs color intensity (*R* value) acquired by the RGB model, (e) TAC detection in fresh oranges, tangerines, lemons, and five common commercial beverages. (Error bar represents the standard deviation of three independent measurements).

erarity over 0–320 μM AA, with a calculated detection limit (LOD) of 3.622 μM based on a signal-to-noise of 3 (Fig. 4(d)). Fig. 4(f) demonstrated the concentration-dependent attenuation of absorbance with the increasing GSH concentration (0–80 μM), indicating the formation of oxTMB was suppressed. Two distinct linear response ranges were observed: 0–32 μM ($R^2 = 0.985$) and 32–80 μM ($R^2 = 0.993$), and the LOD calculated based on the $3\sigma/\text{slope}$ criterion were 0.047 and 1.68 μM , respectively (Fig. 4(g)). Compared to other reported methods for detecting AA and GSH (Tables S2 and S3), the Fe/Mn-N-C-based sensing platform presented in this study featured an enhanced sensitivity and extended linear range.

3.4. TAC assay in actual food samples

TAC serves as a critical biomarker for assessing the integrated efficacy of biological antioxidant systems [17]. It can effectively resist oxidative damage induced by free radicals and exert significant antioxidant effects even at extremely trace concentrations [18]. Therefore, TAC can not only be used to evaluate the activity of antioxidants, but is also widely regarded as an important marker for monitoring the health status of organism. The ability of AA to impede the action of free radicals at low concentrations renders it as a suitable model for the estimation of antioxidants and the calculation of the combined parameters of an-

tioxidants contained within real samples [19]. Therefore, based on the aforementioned colorimetric sensing of AA, a smartphone-assisted platform for assessing TAC levels was established (Fig. 5(a)).

To validate the selectivity of the colorimetric assay for monitoring TAC, various interfering substances were added to the buffer system, including Ca^{2+} , Mg^{2+} , K^+ , Na^+ , glucose, fructose, maltose, lactose, L-lysine, L-arginine, L-tyrosine, L-threonine, and L-isoleucine, each at a concentration ten times that of AA. A substantial absorbance reduction was observed only accompanied by AA or GSH (Fig. 5(b)). Hence, this detection system exhibited excellent selectivity and interference resistance, further confirming the validity of its analytical results. The established smartphone-based TAC detection platform captured high-resolution photos with different absorbances and converted them into RGB color intensities (Fig. 5(c)). The *R* value exhibited the most significant response variation in RGB analysis (Fig. 5(d)). Consequently, a linear calibration model correlating *R* value with AA concentration was established and provided optimal quantification sensitivity. Therefore, this platform enabled easy in-situ TAC analysis using a smartphone, without the need for large-scale equipment.

To further validate the practicality of this colorimetric platform for TAC assessment, the TAC content was determined in three fresh fruits such as oranges, tangerines, and lemons, as well as five commercial beverages. As shown in Fig. 5(e), lemons exhibited relatively higher TAC content among the three fruits. Among the five commercial beverages, four showed higher TAC levels, possibly due to the presence of antioxidants added during beverage production. The above findings validated the potential of nanozymes-based sensing platform for TAC analysis in real samples.

4. Conclusion

In summary, a cage-confined synthesis strategy was employed to fabricate Fe/Mn-N-C dual-single-atom nanozyme. Synergistic effects between Fe-Mn sites uniquely reduced the H_2O_2 activation barrier, endowing superior peroxidase-like activity than Mn-N-C or Fe-N-C monometallic analogues. The enhanced nanozyme kinetics enabled mechanistic discrimination of antioxidant inhibition pathways: AA operated via preferentially react with ROS, while GSH followed active-site coordination. Leveraging this foundation, we developed a smartphone colorimetric platform for on-site total antioxidant capacity assessment and successfully quantified TAC in complex matrices including fruit juices and commercial beverage. This work not only provides new insights to the fabricate high-performance single-atom nanozymes but also expands their applications in evaluating food nutritional value.

Declaration of Competing Interest

The authors declare that they have no competing financial interests or personal relationships that may have influenced the work reported in this study.

CRedit authorship contribution statement

Bingsong Yan: Writing – original draft, Methodology, Data curation. **Yuanjie Zhang:** Investigation, Formal analysis. **Yizhong Lu:** Supervision, Conceptualization. **Zongming Liu:** Project administration, Funding acquisition. **Jinkai Li:** Writing – review & editing.

Acknowledgements

We appreciate the financial support from the “New Universities 20” Foundation of Jinan (Grant No 2021GXRCO99, T202204).

Supplementary materials

Supplementary material associated with this article can be found, in the online version, at doi:10.1016/j.chphma.2025.09.001.

References

- [1] Y. Miao, M. Xia, C. Tao, J. Zhang, P. Ni, Y. Jiang, Y. Lu, Iron-doped carbon nitride with enhanced peroxidase-like activity for smartphone-based colorimetric assay of total antioxidant capacity, *Talanta* 267 (2024) 125141, doi:10.1016/j.talanta.2023.125141.
- [2] G. Liu, H. Zhou, Q. Che, B. Liu, J. Li, B. Cao, Z. Liu, A novel phosphor of Cu^+ -doped PbBrOH : Preparation, luminescence mechanism, and outstanding properties, *J. Mater. Chem. C* 9 (2021) 9178–9187, doi:10.1039/D1TC01855H.
- [3] D. Li, J. Jiang, D. Han, X. Yu, K. Wang, S. Zang, D. Lu, A. Yu, Z. Zhang, Measurement of antioxidant capacity by electron spin resonance spectroscopy based on copper(II) reduction, *Anal. Chem.* 88 (2016) 3885–3890, doi:10.1021/acs.analchem.6b00049.
- [4] G.L. Chen, S.G. Chen, Y. Xiao, N.L. Fu, Antioxidant capacities and total phenolic contents of 30 flowers, *Ind. Crops Prod.* 111 (2018) 430–445, doi:10.1016/j.indcrop.2017.10.051.
- [5] S. Chu, M. Xia, P. Xu, D. Lin, Y. Jiang, Y. Lu, Single-atom Fe nanozymes with excellent oxidase-like and laccase-like activity for colorimetric detection of ascorbic acid and hydroquinone, *Anal. Bioanal. Chem.* 416 (2024) 6067–6077, doi:10.1007/s00216-023-05077-9.
- [6] S. Chu, M. Xia, P. Xu, X. Zhang, W. Liu, Y. Lu, Fe-N-C oxidase-mimicking nanozymes for discrimination of antioxidants and detection of Hg^{2+} , *Anal. Methods* 17 (2025) 3145–3151, doi:10.1039/D5AY00313J.
- [7] Y. Wang, R. Zeng, S. Tian, S. Chen, Z. Bi, D. Tang, D. Knopp, Bimetallic single-atom nanozyme-based electrochemical-photothermal dual-function portable immunoassay with smartphone imaging, *Anal. Chem.* 96 (2024) 13663–13671, doi:10.1021/acs.analchem.4c02606.
- [8] Y.W. Mao, J. Zhang, R. Zhang, J.Q. Li, A.J. Wang, X.C. Zhou, J.J. Feng, N-doped carbon nanotubes supported Fe-Mn dual-single-atoms nanozyme with synergistically enhanced peroxidase activity for sensitive colorimetric detection of acetylcholinesterase and its inhibitor, *Anal. Chem.* 95 (2023) 8640–8648, doi:10.1021/acs.analchem.3c01070.
- [9] G. Ye, Q. He, S. Liu, K. Zhao, Y. Su, W. Zhu, R. Huang, Z. He, Cage-confinement of gas-phase ferrocene in zeolitic imidazolate frameworks to synthesize high-loading and atomically dispersed Fe-N codoped carbon for efficient oxygen reduction reaction, *J. Mater. Chem. A* 7 (2019) 16508–16515, doi:10.1039/C9TA04954A.
- [10] W. Liu, L. Chu, C. Zhang, P. Ni, Y. Jiang, B. Wang, Y. Lu, C. Chen, Hemin-assisted synthesis of peroxidase-like Fe-N-C nanozymes for detection of ascorbic acid-generating bio-enzymes, *Chem. Eng. J.* 415 (2021) 128876, doi:10.1016/j.cej.2021.128876.
- [11] W. Ye, S. Chen, Y. Lin, L. Yang, S. Chen, X. Zheng, Z. Qi, C. Wang, R. Long, M. Chen, J. Zhu, P. Gao, L. Song, J. Jiang, Y. Xiong, Precisely tuning the number of Fe atoms in clusters on N-doped carbon toward acidic oxygen reduction reaction, *Chem* 5 (2019) 2865–2878, doi:10.1016/j.chempr.2019.07.020.
- [12] D. Wu, Z. Zhuo, Y. Song, P. Rao, J. Luo, J. Li, P. Deng, J. Yang, X. Wu, X. Tian, Synergistic spin-valence catalysis mechanism in oxygen reduction reactions on Fe-N-C single-atom catalysts, *J. Mater. Chem. A* 11 (2023) 13502–13509, doi:10.1039/D3TA00555K.
- [13] Y. Yang, L. Chen, Z. Guo, S. Liu, P.-D. Wu, Z. Fang, K. Zhang, H. Li, Remote p-d orbital hybridization via first/second-layer coordination of Fe single atoms with heteroatoms for enhanced electrochemical CO_2 -to- CO reduction, *J. Mater. Chem. A* 12 (2024) 8991–9001, doi:10.1039/D3TA08021H.
- [14] Z. Chen, G. Zhang, Y. Wen, N. Chen, W. Chen, T. Regier, J. Dynes, Y. Zheng, S. Sun, Atomically dispersed Fe-Co bimetallic catalysts for the promoted electroreduction of carbon dioxide, *Nano-Micro Lett.* 14 (2021) 25, doi:10.1007/s40820-021-00746-9.
- [15] C. Chen, W. Liu, P. Ni, Y. Jiang, C. Zhang, B. Wang, J. Li, B. Cao, Y. Lu, W. Chen, Engineering two-dimensional Pd nanoplates with exposed highly active {100} facets toward colorimetric acid phosphatase detection, *ACS Appl. Mater. Interfaces* 11 (2019) 47564–47570, doi:10.1021/acsami.9b16279.
- [16] L. Cui, H. Li, W. Shi, Y. Jing, S. Sun, S. Ai, Z. Guo, The coordination effect of organic ligands in Ce-MOF brings about atomically dispersed Fe in CeO_2 for TAC detection in commercial samples, *Talanta* 285 (2025) 127405, doi:10.1016/j.talanta.2024.127405.
- [17] J. Dan, Z. Su, B. Sun, J. Wang, W. Zhang, A polymetallic nanozyme with high peroxidase mimetic activity for rapid evaluation of total antioxidant capacity, *Microchem. J.* 185 (2023) 108302, doi:10.1016/j.microc.2022.108302.
- [18] S. Zhu, Z. Li, F. Zhang, F. Liu, P. Ni, C. Chen, Y. Jiang, Y. Lu, Single-atom cobalt catalysts as highly efficient oxidase mimics for time-based visualization monitoring the TAC of skin care products, *Chem. Eng. J.* 456 (2023) 141053, doi:10.1016/j.cej.2022.141053.
- [19] L. Cui, W. Shi, H. Li, X. Zhao, S. Ai, X. Meng, S. Sun, Z. Guo, Rod-like Ce-MOF derived spindle-shaped Cu-CeO₂ sheet for total antioxidant capacity detection, *Microchem. J.* 210 (2025) 112955, doi:10.1016/j.microc.2025.112955.